



OPEN

Dynamical behaviour of ultrathin [CoFeB (t_{CoFeB})/Pd] films with perpendicular magnetic anisotropy

Ana S. Silva¹, Simão P. Sá¹, Sergey A. Bunyaev¹, Carlos Garcia², Iñigo J. Sola³, Gleb N. Kakazei¹, Helder Crespo¹ & David Navas⁴✉

CoFeB-based ultrathin films with perpendicular magnetic anisotropy are promising for different emerging technological applications such as nonvolatile memories with low power consumption and high-speed performance. In this work, the dynamical properties of [CoFeB (t_{CoFeB})/Pd (10 Å)]₅ multilayered ultrathin films ($1 \text{ \AA} \leq t_{\text{CoFeB}} \leq 5 \text{ \AA}$) are studied by using two complementary methods: time-resolved magneto-optical Kerr effect and broadband ferromagnetic resonance. The perpendicular magnetization is confirmed for multilayers with $t_{\text{CoFeB}} \leq 4 \text{ \AA}$. The effective perpendicular magnetic anisotropy reaches a clear maximum at $t_{\text{CoFeB}} = 3 \text{ \AA}$. Further increase of CoFeB layer thickness reduces the perpendicular magnetic anisotropy and the magnetization became in-plane oriented for $t_{\text{CoFeB}} \geq 5 \text{ \AA}$. This behaviour is explained by considering competing contributions from surface and magnetoelastic anisotropies. It was also found that the effective damping parameter α_{eff} decreases with CoFeB layer thickness and for $t_{\text{CoFeB}} = 4 \text{ \AA}$ reaches a value of ~ 0.019 that is suitable for microwave applications.

Since the mid 1970s^{1,2}, materials with perpendicular magnetic anisotropy (PMA) have been studied for a large diversity of applications including, but not limited to, perpendicular recording media^{1–4}, patterned magnetic media^{5,6}, high-density spin-transfer torque magnetic random access memories (STT-MRAM)^{7–9} and more recently in skyrmion-based devices^{10–12} and synthetic antiferromagnets for biomedical applications^{13–15}.

Among different materials, CoFeB-based thin films have received great attention since 2010, when Ikeda et al.⁹ demonstrated that this alloy in contact with a MgO layer can show PMA. This behaviour can be achieved when the CoFeB layer is thin enough, and the CoFeB/MgO interfacial anisotropy contribution^{9,16,17} overcomes the volumetric terms of the anisotropy energy¹⁸. Afterwards, several works have been focused on the optimization of the PMA in CoFeB thin films by using different materials for the capping and/or buffer layers¹⁹, including Ta^{20,21}, Hf^{22,23}, Mo^{24,25}, Ru^{26,27}, V²⁶, Nb²⁷, Pt^{28,29}, Pd^{30–32} and Au³³.

Moreover, CoFeB alloys show higher spin polarization than Co, Fe and Ni (up to 65% vs. around 45%)³⁴, and can be grown with a tuned damping parameter (α)^{9,35}. Since damping determines the temporal performance of magnetic devices such as the timescale for magnetization reversal or spin-transfer-torque (STT) switching, α is a key parameter for the development of several technological applications. In particular, materials with low α have been suggested for high-speed spintronic devices, such as in STT-based systems with low switching and power consumption^{8,36}, as well as in magnetic tunnel junctions (MTJs) with high signal-to-noise ratio⁹, and in magnonic devices³⁷. On the other hand, systems with high α values have been suggested for spin pumping and inverse spin Hall effect applications^{38–40}. Therefore, understanding the behaviour of the α parameter is of particular importance.

Although it was reported that the Gilbert damping (α_{Gilbert}) for Co₄₀Fe₄₀B₂₀ alloy can be as low as 0.004^{41,42}, the estimated effective damping (α_{eff}) increases substantially at low thickness⁹ which is detrimental to the development of STT- and MTJs-based devices. For example, it was reported that 1 or 1.3 nm thick CoFeB layers with

¹Departamento de Física e Astronomia, Faculdade de Ciências, Institute of Physics for Advanced Materials, Nanotechnology and Photonics (IFIMUP), Universidade do Porto, 4169-007 Porto, Portugal. ²Departamento de Física y Centro Científico Tecnológico de Valparaíso-CCTVal, Universidad Técnica Federico Santa María, 2390123 Valparaíso, Chile. ³Laser Applications and Photonics Group, Applied Physics Department, University of Salamanca, 37008 Salamanca, Spain. ⁴Instituto de Ciencia de Materiales de Madrid, ICMM-CSIC, 28049 Madrid, Spain. ✉email: davidnavasotero@gmail.com

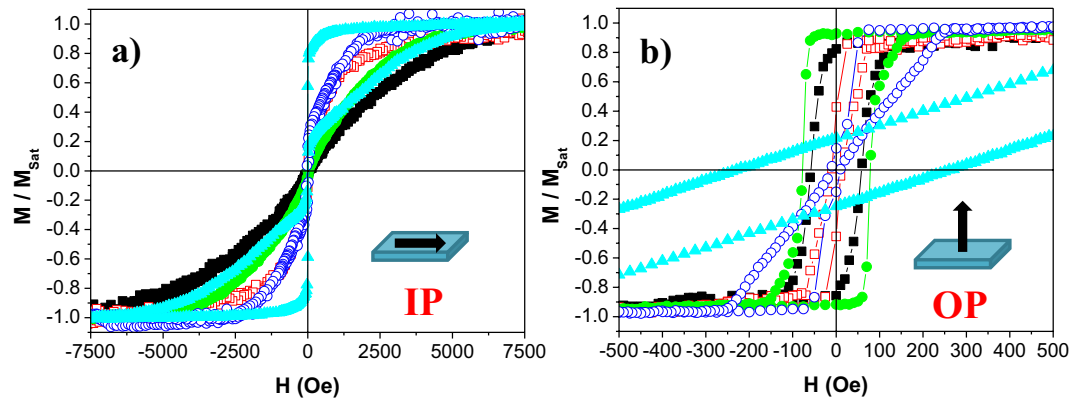


Figure 1. In-plane (a) and out-of-plane (b) hysteresis loops of $[\text{CoFeB } (t_{\text{CoFeB}})/\text{Pd } (10 \text{ \AA})]_5$ multilayer thin films with $t_{\text{CoFeB}} = 1$ (Black filled square), 2 (red open square), 3 (green filled circle), 4 (dark blue open circle) and 5 Å (light blue filled triangle).

PMA show α_{eff} parameters of 0.012³⁵ and 0.027⁹, respectively. This rise has been associated with the fact that the α_{eff} parameter contains contributions from both intrinsic and extrinsic terms⁴³. The intrinsic term or α_{Gilbert} is constant with the resonance frequency but shows temperature dependence^{43,44}. Devolder et al.³⁵ studied the correlation between α_{Gilbert} and the g-factor (g) in CoFeB thin films as a function of the alloy composition and annealing conditions. As it was expected in transition metals, the dependence $\alpha_{\text{Gilbert}} \approx (g - 2)^2$ was reported⁴⁵.

On the other hand, it has been suggested that the extrinsic term can be due to different effects such as⁴⁶:

1. An inhomogeneity contribution based on the local variations of the magnetization and/or the magnetic anisotropy field due to structural defects and/or thickness variations⁴³. In particular, Devolder et al.³⁵ studied the damping parameter of $\text{Co}_x\text{Fe}_{80-x}\text{B}_{20}$ ultrathin films and reported that the inhomogeneity term should be constant with the resonance frequency while it should depend on the sample composition, thickness, and materials used for the capping and/or buffer layers.
2. A two-magnon scattering (TMS) contribution^{47,48}. Regarding this term, Liu et al.⁴¹ performed out-of-plane angular dependence FMR measurements of CoFeB thin films, and they reported that the damping mechanism depends on the layer thickness. It was suggested that α_{eff} is mainly governed by the Gilbert damping in thicker (≥ 4 nm) CoFeB films, while inhomogeneous broadening and two-magnon scattering are the main factors for films thinner than 2 nm.
3. A contribution from the spin-pumping effect^{49,50}. Although this effect was first suggested by Berger⁵¹, it was experimentally confirmed by Mizukami et al.^{52,53} that the damping of non-magnetic/magnetic/non-magnetic trilayers depends on the non-magnetic material. Large damping parameters were determined when non-magnetic materials with a strong spin-orbit coupling, such as Pt and Pd, were used. Iihama et al.²⁰ investigated the damping parameter of Ta/CoFeB/MgO and Ta/CoFeB/Ta thin films using an all-optical pump-probe method, and they claimed that the enhancement of α_{eff} is caused by the spin pumping effect at the Ta/CoFeB interfaces.
4. Any change in the magnetization of a ferromagnetic material placed on top of a coplanar waveguide (CPW) induces eddy currents. These eddy currents generate a magnetic field in the ferromagnet that opposes the original change and provides a damping mechanism (α_{eddy})^{54,55}. Moreover, the generated eddy currents also affect the CPW, and an extra damping mechanism, known as radiative damping (α_{rad}), should be considered^{56,57}.

Although CoFeB/Pd multilayers with strong PMA were first reported in 2010^{30,31}, subsequent works have been mainly focused on understanding the contributions of the volumetric (K_v) and surface (K_s) anisotropy terms to the PMA as a function of the CoFeB layer thickness and the number of CoFeB/Pd bilayers^{32,58,59}. In this paper, we have studied the dynamical behaviour of ultrathin $[\text{CoFeB } (t_{\text{CoFeB}})/\text{Pd } (10 \text{ \AA})]_5$ films with CoFeB thicknesses ranging from 1 to 5 Å by using both vector network analyzer based ferromagnetic resonance (VNA-FMR) and time-resolved magneto-optical Kerr effect (TR-MOKE) measurements. We observed that PMA was achieved for $t_{\text{CoFeB}} \leq 4$ Å, and both K_v and K_s were estimated. In addition, we have performed a systematic study of previously unreported characteristic magnetic parameters such as the CoFeB saturation magnetization and the damping parameter in ultrathin CoFeB/Pd films. Moreover, the effective damping parameter and its related intrinsic and extrinsic contributions were analyzed as a function of t_{CoFeB} .

Results and discussion

Figure 1a and b show the in-plane and out-of-plane hysteresis loops of the $[\text{CoFeB } (t_{\text{CoFeB}})/\text{Pd } (10 \text{ \AA})]_5$ multilayer stacks, respectively. The loops indicated that our samples show PMA when the CoFeB thickness (t_{CoFeB}) ranged from 1 to 4 Å. However, the easy magnetization axis lays in-plane for the largest t_{CoFeB} (5 Å).

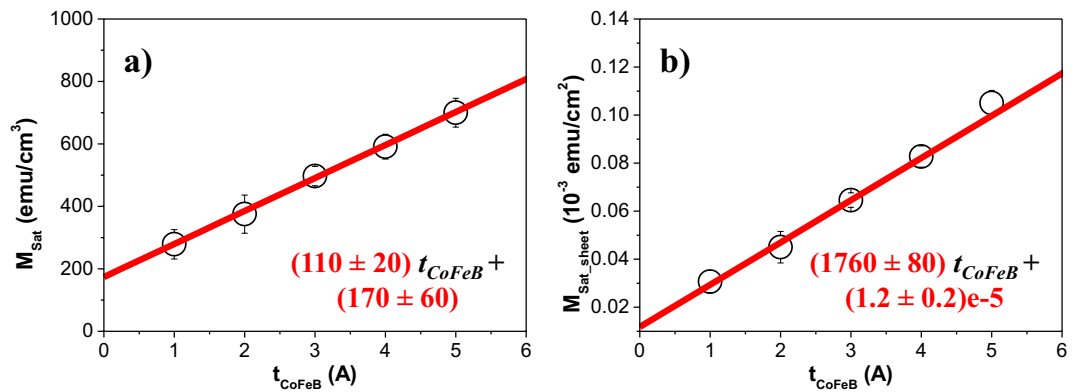


Figure 2. (a) Saturation magnetization, M_{Sat} as a function of the CoFeB layer thickness (t_{CoFeB}). (b) M_{Sat_sheet} as a function of the CoFeB layer thickness (t_{CoFeB}). The continuous red lines are linear fits.

Magnetic moment. Moreover, the hysteresis loops were used to obtain the values of the saturation magnetization (M_{Sat}), which are shown in Fig. 2a. We observed that M_{Sat} increases with the CoFeB film thickness from (280 ± 50) to (700 ± 50) emu/cm^3 for $t_{CoFeB} = 1$ and 5 Å , respectively. This behavior was already observed in ultrathin films, such as for example in Pt/Co/Pt⁶⁰, Ta/CoFeB ($t \text{ nm}$)/SiO₂ ($t = 1, 2, 3, 4, 6, 10, 13 \text{ nm}$)⁶¹, [Co ($t \text{ nm}$)/Pd]₈⁶² and [CoFeB ($t \text{ nm}$)/Pd (1.0 nm)]₁₀ ($t = 0.4, 0.6, 0.8, 1.0$ and 1.2 nm) multilayer films³² with perpendicular anisotropy.

As the CoFeB thickness was varied, while both the Pd thickness (1 nm) and the number of CoFeB/Pd bilayers (5) were kept constant, the rise of M_{Sat} with the CoFeB film thickness could be associated with the increase of the volume magnetic moment contribution while the surface/interface magnetization term should remain constant³². Therefore, the experimental magnetization data can be fitted by a linear dependence (the continuous line in Fig. 2a) and the surface/interface magnetization term can be estimated from the extrapolation of this linear dependence to zero thickness. Our analysis determined that the surface/interfacial magnetization of CoFeB/Pd interfaces is (170 ± 60) emu/cm^3 , which agrees with the value of (180 ± 10) emu/cm^3 reported by Ngo et al.³².

In addition, the magnetization per unit area (M_{Sat_sheet}) vs. the CoFeB film thickness (t_{CoFeB}) is shown in Fig. 2b. As described by Engel et al.⁶³, M_{Sat_sheet} in superlattices can be estimated from

$$M_{Sat_sheet} = I/(N \times A) = M_{eff_CoFeB} \times t_{CoFeB} + M_{eff_Pd} \times t_{Pd} \quad (1)$$

where I is the measured magnetic moment, N is the number of bilayers, A is the area of the films (determined from the software analysis of digital photographs of the samples), M_{eff_CoFeB} is the effective CoFeB saturation magnetization, t_{CoFeB} is the CoFeB layer thickness, M_{eff_Pd} is the effective magnetization of the polarized Pd induced by the ferromagnetic proximity effect^{63–65}, and t_{Pd} is the Pd layer thickness (10 Å). A linear fit of (M_{Sat_sheet} vs. t_{CoFeB}) is also plotted in Fig. 2b. Assuming that the magnetic moment is uniformly induced in the entire Pd layer, $M_{eff_Pd} = (120 \pm 20)$ emu/cm^3 was estimated from the extrapolation of the linear fit to zero CoFeB layer thickness ($t_{CoFeB} = 0 \text{ Å}$). This saturation magnetization is in good agreement with previous studies on Co/Pd multilayers^{64–66}. Additionally, an effective CoFeB saturation magnetization value of $M_{eff_CoFeB} = (1760 \pm 80)$ emu/cm^3 was obtained from the linear fit slope.

This value seems to be too large in comparison with the values previously reported for Co₄₀Fe₄₀B₂₀ thin films and estimated from the hysteresis loops (1000³⁰ or 1034 emu/cm^3 ^{31,67}), ferromagnetic resonance measurements (1019 emu/cm^3 ³⁶⁸) or the linear fit of the magnetization per unit area (M_{Sat_sheet}) vs the CoFeB film thickness (1120⁶⁹, 1150²⁵ or 1200 emu/cm^3 ²⁶). Usually, such large M_{Sat} values have been reported for CoFeB alloys fabricated with lower B concentration, such as ≈ 1670 and 1830 emu/cm^3 for (Co₃₅Fe₆₅)₉₀B₁₀ and (Co₃₅Fe₆₅)_{87.5}B_{2.5} respectively⁷⁰, or in CoFeB multilayers in which the boron atoms diffused out of the CoFeB alloy due to the application of an annealing process (1900 emu/cm^3 for Ta/Co₄₀Fe₄₀B₂₀/MgO multilayers)⁷¹. However, in 2013, Sinha et al.⁷² studied the perpendicular magnetic anisotropy in Ta/CoFeB ($t \text{ nm}$)/MgO multilayers with CoFeB thickness ranging from 0.8 to 5 nm. In agreement with the literature, they reported that the linear fit slope of (M_{Sat_sheet} vs. t) provides an effective CoFeB saturation magnetization of $M_{eff_CoFeB} = 1210 \text{ emu/cm}^3$ for thicker samples ($t \geq 2.2 \text{ nm}$). But large M_{eff_CoFeB} values, such as 1790 emu/cm^3 , were determined for the thinnest CoFeB layers ($t \leq 2.2 \text{ nm}$). Therefore, it was suggested that the effective saturation magnetization increases from its bulk value below a certain magnetic layer thickness. This behaviour was confirmed in our work as well as in Ref.³², where Ngo et al. reported $M_{eff_CoFeB} = 1550 \text{ emu/cm}^3$ in CoFeB ($t \text{ nm}$)/Pd multilayered thin films.

Anisotropy energy terms. The origin of PMA in ultrathin multilayer stacks, such as (CoFeB/Noble metal) bilayers, is based on the competition between the volumetric (K_v) and surface (K_s) terms of the anisotropy energy¹⁸. To distinguish between both contributions, we performed ferromagnetic resonance measurements when the DC external field was applied perpendicular to the sample plane. In general, the FMR spectrum of a thin film depends significantly on the presence of different anisotropies, such as the magnetocrystalline, shape, magnetoelastic and surface contributions, and it can be described through the Kittel equation^{20,73,74}:

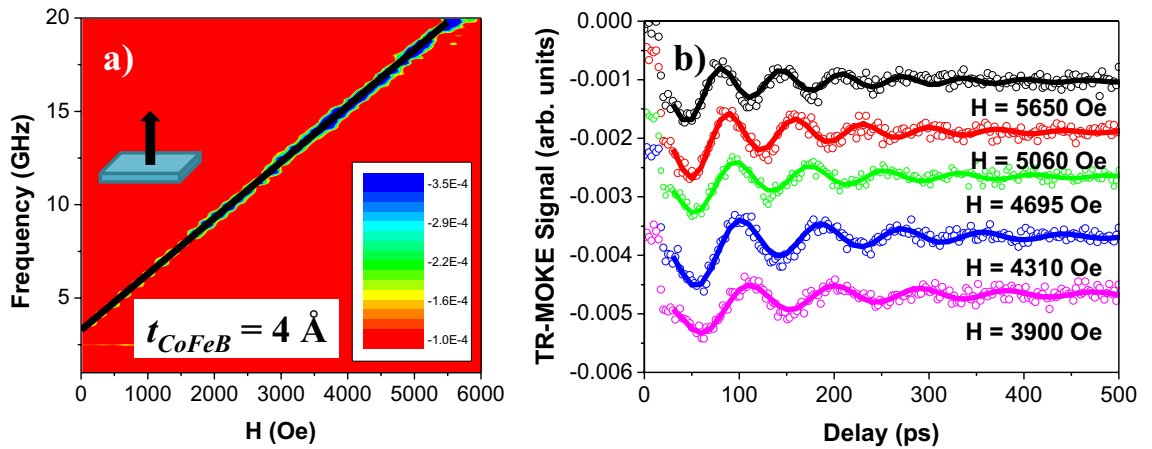


Figure 3. (a) VNA-FMR spectra of the [CoFeB (4 Å)/Pd (10 Å)]₅ multilayer thin film with the external magnetic field applied perpendicularly to the sample plane. The black line corresponds to the fits using the Kittel formula (Eq. 4). (b) Time-resolved magneto-optical Kerr effect (TR-MOKE) signals of a [CoFeB (2 Å)/Pd (10 Å)]₅ multilayer thin film under different external applied fields ($H = 5650, 5060, 4695, 4310$ Oe and 3900 Oe) and when H was applied at $\theta_H = 78^\circ$. Theoretical curves (solid curves) are fits to the experimental data (open symbols) using Eq. (5). Data was moved along the vertical axis for clarity.

$$f_{FMR} = \frac{\gamma}{2\pi} \sqrt{(H \cos(\theta_0 - \theta_H) + H_{eff} \cos^2(\theta_0)) \times (H \cos(\theta_0 - \theta_H) + H_{eff} \cos(2\theta_0))} \quad (2)$$

where $(\gamma/2\pi) = (g\mu_0/h)$ is the gyromagnetic ratio; g is the g-factor; μ_0 is the Bohr magneton; h is Planck's constant; H is the external applied DC magnetic field; H_{eff} is the effective anisotropy field, that is positive for the films with perpendicular magnetization in the absence of external magnetic field and negative for films with in-plane magnetization; θ_H is the angle of the external applied magnetic field and θ_0 is the equilibrium angle of the sample magnetization. The equilibrium angle θ_0 can be derived from the equation:

$$H \sin(\theta_H - \theta_0) = \frac{1}{2} H_{eff} \sin(2\theta_0) \quad (3)$$

When thin films are saturated and $\theta_H = \theta_0$, Eq. (2) can be reduced to⁷⁴:

$$f_{FMR} = \frac{\gamma}{2\pi} (H + H_{eff}) \quad \text{for perpendicular geometry} \quad (4)$$

Figure 3a shows the perpendicular VNA-FMR spectrum of the [CoFeB (4 Å)/Pd (10 Å)]₅ multilayer thin film with PMA as well as a black line, which corresponds to the fits using the Kittel formula (Eq. 4).

However, we should note that we were not able to achieve a good signal-to-noise ratio from samples with the thinnest CoFeB thicknesses ($t_{CoFeB} = 1-3$ Å). For these samples, our analyses were complemented by performing TR-MOKE measurements. All-optical pump-probe technique has been successfully used for understanding the dynamical response of the ultrafast magnetization, the magnetization precession and the effective damping, in materials with perpendicular anisotropy such as [Co/Pt]_n^{75,76} and [Co/Pd]₈⁶² multilayers, L1₀-FePt alloy epitaxial thin films⁷³ or Ta/CoFeB/MgO(Ta) thin films²⁰. As an example, Fig. 3b shows the TR-MOKE signals for [CoFeB (2 Å)/Pd (10 Å)]₅ and as a function of the external applied magnetic field. An ultrafast demagnetization process on the subpicosecond timescale is observed after the application of the pump pulse, followed by a quick remagnetization stage that shows a precessional response in the last section. Both the ferromagnetic resonance frequency (f_{FMR}) and the damping parameter (α) characterize the oscillatory response of the magnetization and it can be fitted by^{73,77}:

$$\theta = \theta_0 + A \times e^{-t/t_0} + B \times \sin(2\pi f_{FMR} t + \varphi) \times e^{-t/\tau} \quad (5)$$

where θ_0 and A are the background magnitudes, and t_0 is the background recovery time. The final term represents the precessional motion where B, f_{FMR}, φ and τ are the amplitude, frequency, phase, and relaxation time, respectively. A good agreement between the model and the experimental data is shown in Fig. 3 (b) and the fits of the f_{FMR} field-dependence were performed through the set of Eqs. (2) and (3)^{20,73}.

The main results of our VNA-FMR and TR-MOKE fits are summarized in Table 1. The gyromagnetic ratio and g-factor did not show any significant dependence with the CoFeB thickness, and we obtained average values of (2.99 ± 0.03) GHz/kOe and (2.14 ± 0.03) , respectively, in agreement with the literature^{23,35,68,78}.

On the other hand, and as observed in the hysteresis loops, the fitted data of H_{eff} shows a transition from positive values for $t_{CoFeB} \leq 4$ Å, meaning that the multilayer films show perpendicular magnetization in the absence of external magnetic field, to negative ones (with in-plane magnetization) for $t_{CoFeB} = 5$ Å (See Fig. 4a). The sample with perpendicular magnetization and the larger positive H_{eff} values corresponds to the multilayer thin film with $t_{CoFeB} = 3$ Å. Also, we should note that the H_{eff} value for $t_{CoFeB} = 1$ Å is larger than for $t_{CoFeB} \geq 2$ Å. This behavior, in combination with the fact that Co₂₀Fe₆₀B₂₀, with a body-centered-cubic (bcc) crystalline structure, has a lattice

t_{CoFeB} (Å)	M_{sat} (emu/cm ³)	$\gamma/2\pi$ (GHz/kOe)	g	H_{eff} (Oe)	K_{eff} (10 ⁵ erg/cm ³)	α_{eff}
1	280 ± 50	—	—	<i>2400 ± 200</i>	<i>3.3 ± 0.8</i>	<i>0.20 ± 0.04</i>
2	380 ± 60	3.01 ± 0.04	2.15 ± 0.03	<i>850 ± 90</i>	<i>1.6 ± 0.4</i>	<i>0.083 ± 0.006</i>
				480 ± 50	0.9 ± 0.2	0.08 ± 0.03
3	500 ± 30	2.96 ± 0.08	2.12 ± 0.06	<i>2630 ± 40</i>	<i>6.5 ± 0.5</i>	<i>0.075 ± 0.004</i>
				2600 ± 200	6.4 ± 0.8	0.06 ± 0.02
4	590 ± 40	3.001 ± 0.006	2.144 ± 0.006	<i>1090 ± 30</i>	<i>3.2 ± 0.3</i>	<i>0.020 ± 0.004</i>
				1100 ± 10	3.2 ± 0.2	0.019 ± 0.001
5	700 ± 50	2.985 ± 0.005	2.133 ± 0.004	−818 ± 5	−2.9 ± 0.2	0.018 ± 0.001

Table 1. Summary of the results for [CoFeB/Pd]_N multilayer systems ($N=5$ bilayers) as a function of the CoFeB thickness (t_{CoFeB}): the saturation magnetization (M_{sat}) extracted from VSM; the gyromagnetic ratio ($\gamma/2\pi$) and g -factor (g) determined from VNA-FMR fits using Eq. (4); Effective anisotropy field (H_{eff}) determined from VNA-FMR (Eq. 4) and TR-MOKE (Eqs. 2, 3 and 5); Effective anisotropy energy (K_{eff}) determined from Eq. (6); The effective damping (α_{eff}) determined from VNA-FMR and TR-MOKE. Data extracted from the VNA-FMR measurements is shown in black. Data extracted from the TR-MOKE measurements is given in *italics and red*.

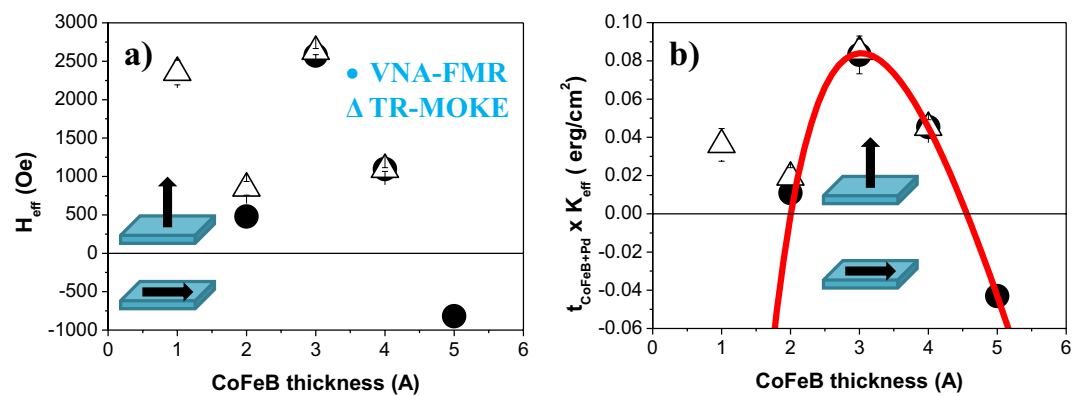


Figure 4. (a) H_{eff} and (b) ($t_{\text{CoFeB}+\text{Pd}} \times K_{\text{eff,CoFeB}}$) as a function of the CoFeB layer thickness ($t_{\text{CoFeB}} = 1 - 5$ Å) for [CoFeB(t_{CoFeB})/Pd(10 Å)]₅ multilayer thin films. While black open circle are the experimental data determined from the VNA-FMR measurements, black open triangle were determined from the TR-MOKE studies. The red solid line in (b) is the fitting to the model described by Eq. (8).

parameter of 2.86 Å⁷⁹, leads us to believe that both the 1 and 2 Å thick CoFeB layers are discontinuous thin films. Even, the continuity of the 3 Å thick CoFeB layers could be in question, which will be suggested below during the discussion related to the damping parameter. So for now, both thinner samples ($t_{\text{CoFeB}} = 1$ and 2 Å) were excluded in the subsequent analysis.

From the fitted data, the effective anisotropy energy (K_{eff}) can be estimated according to (summarized in Table 1):

$$K_{\text{eff}} = \frac{1}{2}(H_{\text{eff}} \times M_{\text{sat}}) \quad (6)$$

Moreover, K_{eff} can be phenomenologically separated into a volume contribution K_v (erg/cm³) and a contribution from the interfaces K_s (erg/cm²), and it can be approximately described by the Néel model⁸⁰:

$$K_{eff} = K_v + (2K_s/t) \quad (7)$$

where the origin of the factor of 2 in the last term is due to the presence of two identical interfaces per magnetic layer, and t is the magnetic layer thickness. Therefore, both K_v and K_s can be obtained by plotting $(t \times K_{eff})$ versus t . According to the Néel model⁸⁰, $(t \times K_{eff})$ should show a linear dependence on t , where K_v is the linear dependence slope, and $2K_s$ corresponds to the intercept with the vertical axis. However, our data shows a deviation from the linear behavior at small CoFeB thicknesses (see Fig. 4b) as already observed in different systems like in Co/Au⁸¹ and Ni/Cu^{82–84} multilayer thin films. This deviation was explained using a phenomenological model that includes the shape anisotropy term, the bulk magnetocrystalline and magnetoelastic anisotropy energies, the surface magnetocrystalline and surface magnetoelastic anisotropy terms⁸³ or the second-order of the magnetoelastic contribution⁸⁴.

More recently, this non-linearity was also reported for NM/CoFeB/MgO thin films (where NM was Ta⁶⁹ or Hf²³) and it was fitted using the equation proposed by Gowtham et al.⁶⁹:

$$K_{eff} \times t = K_v^{eff} \times t + 2 \times K_s^{eff} + (K_3/t) \quad (8)$$

where K_v^{eff} is the effective volumetric contribution that should include the shape anisotropy term and both the bulk magnetocrystalline and bulk magnetoelastic anisotropy energy contributions; K_s^{eff} is the effective surface term that includes the surface magnetocrystalline and magnetoelastic anisotropy terms as well as the second-order term of the bulk magnetoelastic contribution; and coefficient K_3 is related to the second-order term of the surface magnetoelastic contribution.

In agreement with Engel et al.⁶³, we have estimated that $(t_{CoFeB} \times K_{eff,CoFeB}) = (t_{CoFeB+Pd} \times K_{eff})$ where $t_{CoFeB+Pd}$ (t_{CoFeB}) is the thickness of the CoFeB/Pd bilayer (CoFeB layer), K_{eff} is the measured effective anisotropy energy of the [CoFeB/Pd]₅ system and $K_{eff,CoFeB}$ is the effective anisotropy energy of a CoFeB thin film. Therefore, both $K_{v,CoFeB}$ and $K_{s,CoFeB}$ can be obtained by plotting $(t_{CoFeB} \times K_{eff,CoFeB})$ versus t_{CoFeB} (shown in Fig. 4b). Using Eq. (8) to fit the experimental data, we have estimated that $K_{v,CoFeB} = (-16.2 \pm 0.3) \times 10^6$ erg/cm³, $K_{s,CoFeB} = (0.53 \pm 0.01)$ erg/cm² and $K_3 = (-1.48 \pm 0.05) \times 10^{-8}$ erg/cm. Our values are close to the data previously reported in the literature for Hf/CoFeB/MgO²³ and Ta/CoFeB/MgO thin films⁶⁹.

Assuming that the CoFeB layer is amorphous, its bulk magnetocrystalline anisotropy energy contribution should be null. Therefore, we suggest that the volumetric term could be formed by:

$$K_{v,CoFeB} = K_{sh,CoFeB} + K_{me,CoFeB} = (-16.2 \pm 0.3) \times 10^6 \text{ erg/cm}^3 \quad (9)$$

where $K_{sh,CoFeB} = -2\pi M^2_{eff,CoFeB} = (-19 \pm 2) \times 10^6$ erg/cm³ is the shape anisotropy term and $K_{me,CoFeB} = (3 \pm 1) \times 10^6$ erg/cm³ ($= (3 \pm 1) \times 10^5$ J/m³) is the magnetoelastic anisotropy contribution.

As thin films are generally in a state of biaxial stress ($\sigma_x = \sigma_y = \sigma_{in_plane}$ and $\sigma_z = \sigma_{out_of_plane} = 0$), the magnetoelastic anisotropy term can be defined by^{18,85}:

$$K_{me,CoFeB} = \frac{3}{2} \lambda_s \sigma_{in_plane} \quad (10)$$

where λ_s and σ_{in_plane} are the saturation magnetostriction coefficient and the in-plane applied stresses, respectively. Moreover, σ_{in_plane} is related to the in-plane strain ϵ_{in_plane} via the Young's modulus (E) and the Poisson ratio (ν)⁸⁶:

$$\sigma_{in_plane} = \frac{E \epsilon_{in_plane}}{(1 - \nu)} \quad (11)$$

As the magnetoelastic anisotropy term favors that the magnetization lies perpendicular to the sample plane and the saturation magnetostriction coefficient of amorphous Fe₄₀Co₄₀B₂₀ is positive $\lambda_s = 20 \times 10^{-687}$, the magnetic layer should be under tensile stress with $\sigma_{in_plane} \approx (11 \pm 3) \times 10^{10}$ dyne/cm² ($\approx (11 \pm 3)$ GPa). Using the Young's modulus $E = 160 \times 10^{10}$ dyne/cm² ($= 160$ GPa) for CoFeB and the Poisson ratio $\nu = 1/3$ ⁸⁸, the analysis indicates a tensile in-plane strain of $\epsilon_{in_plane} \approx (0.05 \pm 0.01)$. This value is of the same order of magnitude than the strains reported by Gowtham et al.⁶⁹ for Hf/Co₂₀Fe₆₀B₂₀/MgO heterostructures with thicker CoFeB layers. The in-plane tensile strain in our ultrathin films should be related to the large lattice mismatch ($\approx 36\%$)¹⁸ between Pd (3.88 Å)⁸⁹ and CoFeB (2.86 Å for bcc)⁷⁹ lattice parameters.

Effective damping. We then studied the behaviour of the damping parameter (α) as a function of the CoFeB thin film thickness and it was extracted from the frequency linewidths (Δf_{FMR}) in the VNA-FMR spectra. It was experimentally observed that the measured frequency linewidths (Δf_{FMR}) are broadened by extrinsic contributions, which affect the calculations of the damping parameter⁹⁰. Therefore, we used Δf_{FMR} to determine the apparent damping by⁹⁰:

$$\alpha_{app} = \frac{\Delta f_{FMR}}{\left(\frac{\gamma}{2\pi}\right)(2H + H_{eff})} \quad (12)$$

Although α_{app} and the intrinsic damping may differ, we should note that α_{app} should give an upper limit for the intrinsic or Gilbert damping ($\alpha_{Gilbert}$). Open symbols in Fig. 5a and b show the typical curves of the apparent damping versus the external applied magnetic field for the multilayers with $t_{CoFeB} = 4$ and 3 Å, respectively. Although we cannot distinguish between the different extrinsic contributions to the linewidth, it is observed

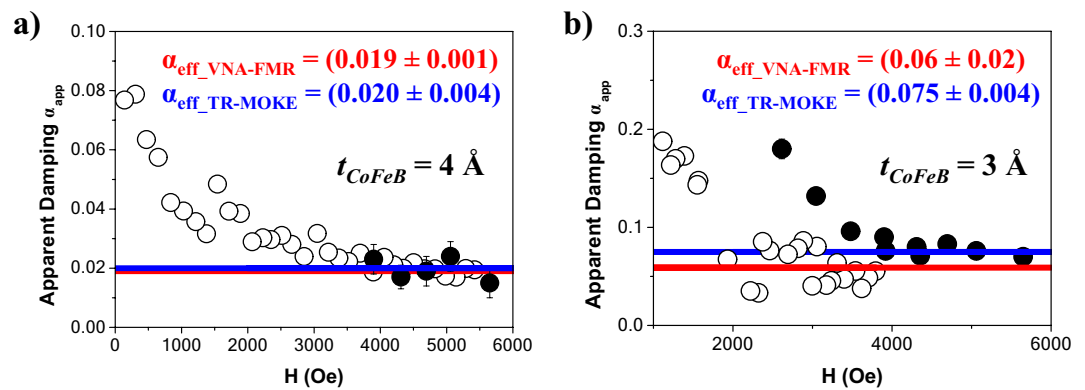


Figure 5. Apparent damping α_{app} as a function of the external applied magnetic field for CoFeB layer thickness of $t_{CoFeB} = 4$ (a) and 3 \AA (b), extracted from VNA-FMR spectra (black open circle) and pump-probe measurements (black filled circle). The red (blue) solid lines are the average of α_{app} determined from the VNA-FMR spectra (pump-probe measurements) for large applied fields and correspond to the α_{eff} .

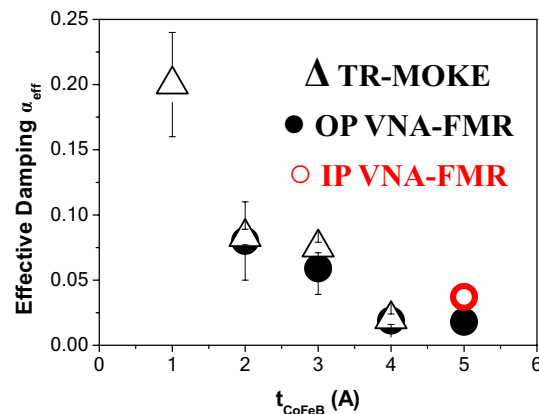


Figure 6. Evolution of the effective damping (α_{eff}) versus t_{CoFeB} and determined from the TR-MOKE measurements (black open triangle), the perpendicular VNA-FMR (black filled circle) and the in-plane VNA-FMR (red open circle) measurements.

that α_{app} approaches a constant value for large applied fields. We have defined this value as the effective damping α_{eff} (see red lines in Figs. 5a and b).

Again, we should note that the signal-to-noise ratio is significantly low for those samples with the thinnest CoFeB thicknesses ($t_{CoFeB} \leq 3 \text{ \AA}$), so optical studies were required to complete our analysis. From the pump-probe measurements, α_{app} can be determined using^{73,91}:

$$\alpha_{app} = \frac{1}{2\pi \times f_{FMR} \times \tau} = \frac{1}{\gamma \times (H + H_{eff}) \times \tau} \quad (13)$$

where f_{FMR} is the resonance frequency and τ is the relaxation time. Both values were fitting parameters in Eq. (5) and they were used to analyze the precessional dynamics (as it was shown in Fig. 3b). Figure 5a and b show the apparent damping versus the external applied magnetic field for multilayers with $t_{CoFeB} = 4$ and 3 \AA , respectively. Again α_{app} approaches a constant value for large applied fields and we assumed that this value is α_{eff} (see blue lines in Fig. 5a and b).

The evolution of the effective damping (α_{eff}) vs. the CoFeB film thicknesses (t_{CoFeB}) obtained by combining both types of measurements is summarized in Table 1 and shown in Fig. 6. It is important to note that both VNA-FMR and pump-probe have provided similar values. As one can see, samples may be separated into two groups: $t_{CoFeB} \leq 3 \text{ \AA}$ and $t_{CoFeB} \geq 4 \text{ \AA}$. For the first group, the value of α_{eff} is large and decreases quickly with thickness increase. It reaches some kind of saturation at $t_{CoFeB} = 4 \text{ \AA}$ and decreases only slightly (by 10%) for $t_{CoFeB} = 5 \text{ \AA}$. As Azzawi et al.⁹² reported in 2016, the non-continuity of thin films leads to the increase of the extrinsic contribution to the damping by adding an extra two-magnon scattering term. Therefore, we have suggested that the increase of α_{eff} for the thinnest CoFeB layers ($t_{CoFeB} \leq 3 \text{ \AA}$) could be related to the abrupt rise of the two-magnon scattering contribution due to the non-continuity of the ultrathin layers.

To better understand the effective damping of the samples with nearly continuous CoFeB layers ($t_{\text{CoFeB}} = 4$ and 5 \AA), we have tried to distinguish different contributions to the damping parameter that were briefly described in the introduction section. Remembering that eddy currents become important when the magnetic film thickness is comparable to or greater than the skin depth⁹⁰, and the radiative damping is proportional to the magnetic layer thickness⁵⁷, neither α_{eddy} nor α_{rad} should have significant contributions in our ultrathin films and they could be ignored. On the other hand, the literature suggests that the two-magnon scattering contribution (α_{TMS}) is minimized in the perpendicular geometry, such as the one mainly used in this work⁹³. In particular, Liu et al.⁴¹ studied the angular dependence of the two-magnon scattering contribution in a CoFeB thin film and confirmed that this effect is suppressed in the perpendicular configuration. They determined that the two-magnon contribution is significant when the sample magnetization angle, relative to the perpendicular direction or 0° , is pointed to an angle larger than 45° . Even α_{TMS} can achieve a value as large as the intrinsic damping in the in-plane configuration. Therefore, the α_{TMS} contribution could also be disregarded and the total measured damping should be mainly composed of the intrinsic term and the spin-pumping contribution:

$$\alpha_{\text{eff}} = \alpha_{\text{Gilbert}} + \alpha_{s-p} \quad (14)$$

The spin-pumping contribution α_{s-p} can be defined using the formula^{94–96}:

$$\alpha_{s-p} = 2g\mu_B \frac{g^{\uparrow\downarrow}}{4\pi M_{\text{eff_CoFeB}} t_{\text{CoFeB}}} \frac{1}{t_{\text{CoFeB}}} \left(1 - e^{-2t_{\text{Pd}}/\lambda_{\text{Pd}}}\right) \quad (15)$$

where g is the g-factor; $\mu_0 = (9.27400915 \times 10^{-21}) \text{ erg/Oe}$ is the Bohr magneton; $M_{\text{eff_CoFeB}} = (1760 \pm 80) \text{ emu/cm}^3$ and t_{CoFeB} are the effective saturation magnetization moment and the thickness of the CoFeB layer, respectively; $g^{\uparrow\downarrow}$ is the CoFeB/Pd interface spin mixing conductance; $t_{\text{Pd}} = 0.5 \text{ nm}$ is half the Pd layer thickness and $\lambda_{\text{Pd}} = 9 \text{ nm}$ ⁹⁵ is the spin diffusion length for Pd layer. The factor of 2 is related to the fact that the CoFeB layer is sandwiched by two Pd layers.

Considering the damping value for $t_{\text{CoFeB}} = 4 \text{ \AA}$ ($\alpha_{\text{eff}} = (0.019 \pm 0.001)$) and assuming that $\alpha_{\text{Gilbert}} = 0.004$ ^{41,42,97}, we have estimated that $\alpha_{s-p} \approx (0.015 \pm 0.001)$. From Eq. (15), the CoFeB/Pd interface spin mixing conductance value should be $g^{\uparrow\downarrow} \approx (3 \times 10^{15}) \text{ cm}^{-2}$. Although this is a rough estimation, $g^{\uparrow\downarrow}$ is of the same order of magnitude than the values already reported in the literature, particularly $2.21 \times 10^{15} \text{ cm}^{-2}$ for a CoFeB/Pd interface⁹⁸ or $0.722 \times 10^{15} \text{ cm}^{-2}$ for a β -Ta/CoFeB interface⁶¹.

Finally, we estimated the two-magnon term (α_{TMS}) for the sample with the most perfectly continuous CoFeB layers, namely the one with $t_{\text{CoFeB}} = 5 \text{ \AA}$. As it was mentioned above, α_{TMS} is negligible in the perpendicular geometry but can have an important contribution in the in-plane configuration. Therefore, for this sample we have compared the damping parameter, determined from in-plane VNA-FMR measurement (shown in Fig. 6) with the perpendicular one. While $\alpha_{\text{eff}}^{\text{OP}} = (0.018 \pm 0.001)$, the in-plane value is $\alpha_{\text{eff}}^{\text{IP}} = (0.037 \pm 0.008)$. Assuming that the difference between both values is due to the two-magnon contribution, we estimated that $\alpha_{\text{TMS}} = (0.019 \pm 0.005)$, confirming the importance of α_{TMS} in the in-plane configuration and in agreement with literature⁴¹.

Summarizing, we have studied the magnetic behaviour of [CoFeB/Pd]₅ multilayered thin films using two complementary techniques. The thicknesses of the CoFeB films reported in the literature have usually ranged between 0.5 nm to a few tens of nm. Here, we focused our attention in multilayers where t_{CoFeB} was varied between 1 and 5 \AA . Our analysis determined an increase of the effective saturation magnetization from its bulk value to $M_{\text{eff_CoFeB}} = (1760 \pm 80) \text{ emu/cm}^3$. PMA was observed in the as-cast samples for CoFeB layer thickness $\leq 4 \text{ \AA}$. This behaviour was modeled by considering volumetric and surface anisotropy contributions. Then, we confirmed the presence of a strong surface anisotropy contribution as well as a magnetoelastic anisotropy term. This last term suggests that our ultrathin CoFeB films are under in-plane tensile strain. Finally, an effective damping parameter as low as $\alpha_{\text{eff}} \approx (0.019 \pm 0.001)$ was observed for the multilayer with 4 \AA CoFeB thickness. We suggested that for $t_{\text{CoFeB}} \geq 4 \text{ \AA}$ the layer is continuous and the main contribution to effective damping is coming from spin-pumping when for lower thicknesses α_{eff} is dominated by two-magnon scattering.

Methods

[CoFeB (t_{CoFeB})/Pd (10 \AA)]₅ multilayer thin films were sandwiched between a Ta(20 \AA)/Pd(20 \AA) seed bilayer and a 50 \AA Pd capping layer. Samples were deposited at room temperature on Si(100) substrates using confocal dc magnetron sputtering with a base pressure below 2×10^{-10} Torr and an Ar working gas pressure of 5 mTorr (more details are given in Ref.⁵⁸). The CoFeB layer thickness (t_{CoFeB}) was varied between 1 and 5 \AA and this alloy was sputtered from a $\text{Co}_{40}\text{Fe}_{40}\text{B}_{20}$ target.

While room temperature magnetic hysteresis loops were measured in a vibrating sample magnetometer (VSM), the dynamical behaviour was studied by comparing TR-MOKE and VNA-FMR measurements. FMR measurements were carried out at room temperature using a coplanar waveguide (CPW) connected to a vector network analyzer. The samples were placed film down on the CPW, and the complex S_{21} parameter was measured as a function of the external magnetic field over a frequency range up to 20 GHz⁹⁹. The external DC magnetic field (H) was applied along ($\theta_H = 90^\circ$) or perpendicular ($\theta_H = 0^\circ$) to the sample plane for in-plane and perpendicular measurements, respectively, and was always perpendicular to the ac field generated by the CPW. On the other hand, the dynamical response of the magneto-optical signals was obtained by an ultrafast pump-probe system based on a commercial Titanium:sapphire laser amplifier (Femtolasers Compact Pro CE-phase) delivering sub-30-fs laser pulses (approximately 40 nm bandwidth centered at 800 nm) with $\sim 1 \text{ mJ}$ of energy at a repetition rate of 1 kHz and with carrier-envelope phase (CEP) stabilization capability, seeded by a CEP-stabilised ultrafast laser oscillator (Femtolasers Rainbow). Time-resolved measurements were performed in polar MOKE configuration using 0.7% and 99.3% of the pulse energy for the probe and pump pulses, respectively. The spot size ratio between

the pump and probe beams was adjusted to be 4:1 to assure that the probe spot hits a homogeneous pump illuminated area of the sample, and the pump fluence was fixed to 2 mJ/cm². In order to increase the signal-to-noise ratio of the TR-MOKE signal, the external DC magnetic field was applied at an angle of $\theta_H = 78^\circ$ ¹⁰⁰. All-optical measurements were performed under ambient conditions.

Received: 22 June 2020; Accepted: 1 December 2020

Published online: 08 January 2021

References

- Iwasaki, S. & Nakamura, Y. The magnetic field distribution of a perpendicular recording head. *IEEE Trans. Magn.* **14**, 436–438 (1978).
- Iwasaki, S., Nakamura, Y. & Ouchi, K. Perpendicular magnetic recording with a composite anisotropy film. *IEEE Trans. Magn.* **61**, 1456–1458 (1979).
- Richter, H. J. The transition from longitudinal to perpendicular recording. *J. Phys. D* **40**, R149 (2007).
- Piramanayagam, S. N. & Srinivasan, K. Recording media research for future hard disk drives. *J. Magn. Magn. Mater.* **321**, 485–494 (2009).
- Terris, B. D. & Thomson, T. Nanofabricated and self-assembled magnetic structures as data storage media. *J. Phys. D* **38**, R199 (2005).
- Moser, A., Hellwig, O., Kercher, D. & Dobisz, E. Off-track margin in bit patterned media. *Appl. Phys. Lett.* **91**, 162502 (2007).
- Khvalkovskiy, A. V. *et al.* Basic principles of STT-MRAM cell operation in memory arrays. *J. Phys. D* **46**, 074001 (2013).
- Mangin, S. *et al.* Current-induced magnetization reversal in nanopillars with perpendicular anisotropy. *Nat. Mater.* **5**, 210–215 (2006).
- Ikeda, S. *et al.* A perpendicular-anisotropy CoFeB–MgO magnetic tunnel junction. *Nat. Mater.* **9**, 721–724 (2010).
- Fert, A., Cros, V. & Sampaio, J. Skyrmions on the track. *Nat. Nanotechnol.* **8**, 152–156 (2013).
- Moreau-Luchaire, C. *et al.* Additive interfacial chiral interaction in multilayers for stabilization of small individual skyrmions at room temperature. *Nat. Nanotechnol.* **11**, 444–448 (2016).
- Woo, S. *et al.* Observation of room-temperature magnetic skyrmions and their current-driven dynamics in ultrathin metallic ferromagnets. *Nat. Mater.* **15**, 501–506 (2016).
- Mansell, R. *et al.* Magnetic particles with perpendicular anisotropy for mechanical cancer cell destruction. *Sci. Rep.* **7**, 4257 (2017).
- Vemulkar, T., Mansell, R., Petit, D. C. M. C., Cowburn, R. P. & Lesniak, M. S. Highly tunable perpendicularly magnetized synthetic antiferromagnets for biotechnology applications. *Appl. Phys. Lett.* **107**, 012403 (2015).
- Peixoto, L. *et al.* Magnetic nanostructures for emerging biomedical applications. *Appl. Phys. Rev.* **7**, 011310 (2020).
- Endo, M., Kanai, S., Ikeda, S., Matsukura, F. & Ohno, H. Electric-field effects on thickness dependent magnetic anisotropy of sputtered MgO/Co₄₀Fe₄₀B₂₀/Ta structures. *Appl. Phys. Lett.* **96**, 212503 (2010).
- Bersweiler, M., Sato, H. & Ohno, H. Magnetic and FREE-LAYER PROPERTIES of MgO/(Co)FeB/MgO structures: dependence on CoFeB composition. *IEEE Magn. Lett.* **8**, 3109003 (2017).
- Johnson, M. T., Bloemen, P. J. H., den Broeder, F. J. A. & de Vries, J. J. Magnetic anisotropy in metallic multilayers. *Rep. Prog. Phys.* **59**, 1409–1458 (1996).
- Dieny, B. & Chshiev, M. Perpendicular magnetic anisotropy at transition metal/oxide interfaces and applications. *Rev. Mod. Phys.* **89**, 025008 (2017).
- Iihama, S. *et al.* Gilbert damping constants of Ta/CoFeB/MgO(Ta) thin films measured by optical detection of precessional magnetization dynamics. *Phys. Rev. B* **89**, 174416 (2014).
- Watanabe, K. *et al.* Dependence of magnetic properties of MgO/CoFeB/Ta stacks on CoFeB and Ta thicknesses. *Jpn. J. Appl. Phys.* **54**, 04DM04 (2015).
- Liu, T., Cai, J. W. & Sun, L. Large enhanced perpendicular magnetic anisotropy in CoFeB/MgO system with the typical Ta buffer replaced by an Hf layer. *AIP Adv.* **2**, 032151 (2012).
- Lourembam, J. *et al.* Thickness-dependent perpendicular magnetic anisotropy and gilbert damping in Hf/Co₂₀Fe₆₀B₂₀/MgO heterostructures. *Phys. Rev. Appl.* **10**, 044057 (2018).
- Liu, T., Zhang, Y., Cai, J. W. & Pan, H. Y. Thermally robust Mo/CoFeB/MgO trilayers with strong perpendicular magnetic anisotropy. *Sci. Rep.* **4**, 5895 (2014).
- Watanabe, K., Fukami, S., Sato, H., Matsukura, F. & Ohno, H. Magnetic properties of CoFeB–MgO stacks with different buffer-layer materials (Ta or Mo). *IEEE Trans. Magn.* **52**, 3400904 (2016).
- Natarajarathinam, A. *et al.* Influence of capping layers on CoFeB anisotropy and damping. *J. Appl. Phys.* **112**, 053909 (2012).
- Lee, D.-S., Chang, H.-T., Cheng, C.-W. & Chern, G. Perpendicular magnetic anisotropy in MgO/CoFeB/Nb and a comparison of the cap layer effect. *IEEE Trans. Magn.* **50**, 3201904 (2014).
- Malinowski, G., Kuiper, K. C., Lavrijsen, R., Swagten, H. J. M. & Koopmans, B. Magnetization dynamics and Gilbert damping in ultrathin Co₄₈Fe₃₂B₂₀ films with out-of-plane anisotropy. *Appl. Phys. Lett.* **94**, 102501 (2009).
- Lee, D.-Y., Shim, T.-H. & Park, J.-G. Effects of Pt capping layer on perpendicular magnet anisotropy in pseudo-spin valves of Ta/CoFeB/MgO/CoFeB/Pt magnetic-tunneling junctions. *Appl. Phys. Lett.* **102**, 212409 (2013).
- Fowley, C. *et al.* Perpendicular magnetic anisotropy in CoFeB/Pd bilayers. *IEEE Trans. Magn.* **46**, 2116 (2010).
- Jung, J. H., Lim, S. H. & Lee, S. R. Strong perpendicular magnetic anisotropy in thick CoFeB films sandwiched by Pd and MgO layers. *Appl. Phys. Lett.* **96**, 042503 (2010).
- Ngo, D.-T. *et al.* Perpendicular magnetic anisotropy and the magnetization process in CoFeB/Pd multilayer films. *J. Phys. D Appl. Phys.* **47**, 445001 (2014).
- Kuświk, P., Głowiński, H., Coy, E., Dubowik, J. & Stobiecki, F. Perpendicularly magnetized Co₂₀Fe₆₀B₂₀ layer sandwiched between Au with low Gilbert damping. *J. Phys. Condens. Matter* **29**, 435803 (2017).
- Huang, S. X., Chen, T. Y. & Chien, C. L. Spin polarization of amorphous CoFeB determined by point-contact Andreev reflection. *Appl. Phys. Lett.* **92**, 242509 (2008).
- Devolder, T. *et al.* Damping of Co_xFe_{80-x}B₂₀ ultrathin films with perpendicular magnetic anisotropy. *Appl. Phys. Lett.* **102**, 022407 (2013).
- Tudosa, I., Katine, J. A., Mangin, S. & Fullerton, E. E. Perpendicular spin-torque switching with a synthetic antiferromagnetic reference layer. *Appl. Phys. Lett.* **96**, 212504 (2010).
- Conca, A. *et al.* Low spin-wave damping in amorphous Co₄₀Fe₄₀B₂₀ thin films. *J. Appl. Phys.* **113**, 213909 (2013).
- Ruiz-Calaforra, A. *et al.* The role of the non-magnetic material in spin pumping and magnetization dynamics in NiFe and CoFeB multilayer systems. *J. Appl. Phys.* **117**, 163901 (2015).
- Correa, M. A. *et al.* Exploring the magnetization dynamics, damping and anisotropy in engineered CoFeB/(Ag, Pt) multilayer films grown onto amorphous substrate. *J. Magn. Magn. Mater.* **485**, 75–81 (2019).

40. Duan, Z. *et al.* Spin-wave modes in permalloy/platinum wires and tuning of the mode damping by spin Hall current. *Phys. Rev. B* **90**, 024427 (2014).
41. Liu, X., Zhang, W., Carter, M. J. & Xiao, G. Ferromagnetic resonance and damping properties of CoFeB thin films as free layers in MgO-based magnetic tunnel junctions. *J. Appl. Phys.* **110**, 033910 (2011).
42. Okada, A. *et al.* Magnetization dynamics and its scattering mechanism in thin CoFeB films with interfacial anisotropy. *PNAS* **114**, 3815–3820 (2017).
43. Farle, M. Ferromagnetic resonance of ultrathin metallic layers. *Rep. Prog. Phys.* **61**, 755–826 (1998).
44. Bhagat, S. M. & Lubitz, P. Temperature variation of ferromagnetic relaxation in the 3d transition metals. *Phys. Rev. B* **10**, 179 (1974).
45. Kambersky, V. On ferromagnetic resonance damping in metals. *Czech. J. Phys. B* **26**, 1366–1383 (1976).
46. Barman, A. & Sinha, J. Magnetic damping. In *Spin Dynamics and Damping in Ferromagnetic Thin Films and Nanostructures* (eds Barman, A. & Sinha, J.) 27–44 (Springer, Berlin, 2018).
47. Lenz, K. *et al.* Two-magnon scattering and viscous Gilbert damping in ultrathin ferromagnets. *Phys. Rev. B* **73**, 144424 (2006).
48. Lindner, J. *et al.* Two-magnon damping in thin films in case of canted magnetization: theory versus experiment. *Phys. Rev. B* **80**, 224421 (2009).
49. Tserkovnyak, Y., Brataas, A. & Bauer, G. E. W. Enhanced Gilbert damping in thin ferromagnetic films. *Phys. Rev. Lett.* **88**, 117601 (2002).
50. Tserkovnyak, Y., Brataas, A. & Bauer, G. E. W. Spin pumping and magnetization dynamics in metallic multilayers. *Phys. Rev. B* **66**, 224403 (2002).
51. Berger, L. Emission of spin waves by a magnetic multilayer traversed by a current. *Phys. Rev. B* **54**, 9353 (1996).
52. Mizukami, S., Ando, Y. & Miyazaki, T. Ferromagnetic resonance linewidth for NM/80NiFe/NM films (NM=Cu, Ta, Pd and Pt). *J. Magn. Magn. Mater.* **226–230**(Part 2), 1640–1642 (2001).
53. Mizukami, S., Ando, Y. & Miyazaki, T. Effect of spin diffusion on Gilbert damping for a very thin permalloy layer in Cu/permalloy/Cu/Pt films. *Phys. Rev. B* **66**, 104413 (2002).
54. Lock, J. M. Eddy current damping in thin metallic ferromagnetic films. *Br. J. Appl. Phys.* **17**, 1645 (1966).
55. van de Riet, E. & Roozeboom, F. Ferromagnetic resonance and eddy currents in high-permeable thin films. *J. Appl. Phys.* **81**, 350–354 (1997).
56. Schoen, M. A. W., Shaw, J. M., Nembach, H. T., Weiler, M. & Silva, T. J. Radiative damping in waveguide-based ferromagnetic resonance measured via analysis of perpendicular standing spin waves in sputtered permalloy films. *Phys. Rev. B* **92**, 184417 (2015).
57. Schoen, M. A. W. *et al.* Ultra-low magnetic damping of a metallic ferromagnet. *Nat. Phys.* **12**, 839–842 (2016).
58. Franco, A. F., Gonzalez-Fuentes, C., Akerman, J. & Garcia, C. Anisotropy constant and exchange coupling strength of perpendicularly magnetized CoFeB/Pd multilayers and exchange springs. *Phys. Rev. B* **95**, 144417 (2017).
59. Franco, A. F. *et al.* Variable variance Preisach model for multilayers with perpendicular magnetic anisotropy. *Phys. Rev. B* **94**, 064431 (2016).
60. Metaxas, P. J. *et al.* Creep and flow regimes of magnetic domain-wall motion in ultrathin Pt/Co/Pt films with perpendicular anisotropy. *Phys. Rev. Lett.* **99**, 217208 (2007).
61. Panda, S. N., Mondal, S., Sinha, J., Choudhury, S. & Barman, A. All-optical detection of interfacial spin transparency from spin pumping in β -Ta/CoFeB thin films. *Sci. Adv.* **5**, eaav7200 (2019).
62. Pal, S., Rana, B., Hellwig, O., Thomson, T. & Barman, A. Tunable magnonic frequency and damping in [Co/Pd]₈ multilayers with variable Co layer thickness. *Appl. Phys. Lett.* **98**, 082501 (2011).
63. Engel, B. N., England, C. D., Van Leeuwen, R. A., Wiedmann, M. H. & Falco, C. M. Interface magnetic anisotropy in epitaxial superlattices. *Phys. Rev. Lett.* **67**, 1910 (1991).
64. Bennett, W. R., England, C. D., Person, D. C. & Falco, C. M. Magnetic properties of Pd/Co multilayers. *J. Appl. Phys.* **69**, 4384–4390 (1991).
65. Wu, R., Li, C. & Freeman, A. J. Structural, electronic and magnetic properties of Co/Pd(111) and Co/Pt(111). *J. Magn. Magn. Mater.* **99**, 71–80 (1991).
66. Obinata, A. *et al.* Electric-field control of magnetic moment in Pd. *Sci. Rep.* **5**, 14303 (2015).
67. Hayakawa, J. *et al.* Current-driven magnetization switching in CoFeB/MgO/CoFeB magnetic tunnel junctions. *Jpn. J. Appl. Phys.* **44**, L1267 (2005).
68. Ranjbar, M. *et al.* CoFeB-based spin hall nano-oscillators. *IEEE Magn. Lett.* **5**, 3000504 (2014).
69. Gowtham, P. G., Stiehl, G. M., Ralph, D. C. & Buhrman, R. A. Thickness-dependent magnetoelasticity and its effects on perpendicular magnetic anisotropy in Ta/CoFeB/MgO thin films. *Phys. Rev. B* **93**, 024404 (2016).
70. Munakata, M., Aoki, S.-I. & Yagi, M. B-concentration dependence on anisotropy field of CoFeB thin film for gigahertz frequency use. *IEEE Trans. Magn.* **41**, 3262–32624 (2005).
71. Fukami, S. *et al.* Current-induced domain wall motion in perpendicularly magnetized CoFeB nanowire. *Appl. Phys. Lett.* **98**, 082504 (2011).
72. Sinha, J. *et al.* Enhanced interface perpendicular magnetic anisotropy in Ta[CoFeB]MgO using nitrogen doped Ta underlayers. *Appl. Phys. Lett.* **102**, 242405 (2013).
73. Mizukami, S. *et al.* Fast magnetization precession observed in L10-FePt epitaxial thin film. *Appl. Phys. Lett.* **98**, 052501 (2011).
74. Kittel, C. On the theory of ferromagnetic resonance absorption. *Phys. Rev.* **73**, 155 (1948).
75. Barman, A. *et al.* Ultrafast magnetization dynamics in high perpendicular anisotropy [Co/Pt]_n multilayers. *J. Appl. Phys.* **101**, 09D102 (2007).
76. Mizukami, S. *et al.* Gilbert damping in perpendicularly magnetized Pt/Co/Pt films investigated by all-optical pump-probe technique. *Appl. Phys. Lett.* **96**, 152502 (2010).
77. Song, H.-S. *et al.* Observation of the intrinsic Gilbert damping constant in Co/Ni multilayers independent of the stack number with perpendicular anisotropy. *Appl. Phys. Lett.* **102**, 102401 (2013).
78. Tu, H. Q. *et al.* Gilbert damping in CoFeB/GaAs(001) film with enhanced in-plane uniaxial magnetic anisotropy. *Sci. Rep.* **7**, 43971 (2017).
79. Park, C. *et al.* Annealing effects on structural and transport properties of rf-sputtered CoFeB/MgO/CoFeB magnetic tunnel junctions. *J. Appl. Phys.* **99**, 08A90 (2006).
80. Néel, L. L'approche à la saturation de la magnétostriction. *J. Phys. Radium* **15**, 376–378 (1954).
81. den Broeder, F. J. A., Hoving, W. & Bloemen, P. J. H. Magnetic anisotropy of multilayers. *J. Magn. Magn. Mater.* **93**, 562–570 (1991).
82. Jungblut, R., Johnson, M. T., van den Stegge, J., Reinders, A. & den Broeder, F. J. A. Orientational and structural dependence of magnetic anisotropy of Cu/Ni/Cu sandwiches: misfit interface anisotropy. *J. Appl. Phys.* **75**, 6424 (1994).
83. Bochi, G. *et al.* Perpendicular magnetic anisotropy, domains, and misfit strain in epitaxial Ni/Cu_{1-x}Ni_x/Cu/Si (001) thin films. *Phys. Rev. B* **52**, 7311 (1995).
84. Ha, K. & O'Handley, R. C. Nonlinear magnetoelastic anisotropy in Cu/Ni/Cu/Si(001) films. *J. Appl. Phys.* **85**, 5282 (1999).
85. Cullity, B. D. & Graham, C. D. *Introduction to the Magnetic Materials* 2nd edn, 258–266 (Wiley, Hoboken, 2009).
86. O'Handley, R. C. *Modern Magnetic Materials* 667–669 (Wiley, New York, 1999).

87. O'Handley, R. C. Magnetostriction of transition-metal-metalloid glasses: Temperature dependence. *Phys. Rev. B* **18**, 930 (1978).
88. Tang, Z. *et al.* Magneto-mechanical coupling effect in amorphous $\text{Co}_{40}\text{Fe}_{40}\text{B}_{20}$ films grown on flexible substrates. *Appl. Phys. Lett.* **105**, 103504 (2014).
89. Arblaster, J. W. Crystallographic properties of palladium. *Platinum Met. Rev.* **56**, 181 (2012).
90. Bilzer, C. Microwave susceptibility of thin ferromagnetic films: metrology and insight into magnetization dynamics (Ph.D. thesis, Université Paris-Sud 11) <https://tel.archives-ouvertes.fr/tel-00202827/document> (2008).
91. Walowski, J. *et al.* Intrinsic and non-local Gilbert damping in polycrystalline nickel studied by Ti : sapphire laser fs spectroscopy. *J. Phys. D Appl. Phys.* **41**, 164016 (2008).
92. Azzawi, S. *et al.* Evolution of damping in ferromagnetic/nonmagnetic thin film bilayers as a function of nonmagnetic layer thickness. *Phys. Rev. B* **93**, 054402 (2016).
93. Hurben, M. J. & Patton, C. E. Theory of two magnon scattering microwave relaxation and ferromagnetic resonance linewidth in magnetic thin films. *J. Appl. Phys.* **83**, 4344–4365 (1998).
94. Shaw, J. M., Nembach, H. T. & Silva, T. J. Determination of spin pumping as a source of linewidth in sputtered $\text{Co}_{90}\text{Fe}_{10}/\text{Pd}$ multilayers by use of broadband ferromagnetic resonance spectroscopy. *Phys. Rev. B* **85**, 054412 (2012).
95. Foros, J., Woltersdorf, G., Heinrich, B. & Brataas, A. Scattering of spin current injected in $\text{Pd}(001)$. *J. Appl. Phys.* **97**, 10A714 (2005).
96. Kato, T. *et al.* Perpendicular anisotropy and Gilbert damping in sputtered Co/Pd multilayers. *IEEE Trans. Magn.* **48**, 3288–3291 (2012).
97. Sato, N., O'Brien, K. P., Millard, K., Doyle, B. & Oguz, K. Investigation of extrinsic damping caused by magnetic dead layer in Ta–CoFeB–MgO multilayers with perpendicular anisotropy. *J. Appl. Phys.* **119**, 093902 (2016).
98. Kim, D.-J., Kim, S.-I., Park, S.-Y., Lee, K.-D. & Park, B.-G. Ferromagnetic resonance spin pumping in CoFeB with highly resistive non-magnetic electrodes. *Curr. Appl. Phys.* **14**, 1344–1348 (2014).
99. Tokac, M. *et al.* Interfacial structure dependent spin mixing conductance in cobalt thin films. *Phys. Rev. Lett.* **115**, 056601 (2015).
100. Lattery, D. M. *et al.* Quantitative analysis and optimization of magnetization precession initiated by ultrafast optical pulses. *Appl. Phys. Lett.* **113**, 162405 (2018).

Acknowledgements

This work was supported by the Portuguese Fundação para a Ciência e a Tecnologia (FCT) and COMPETE 2020 (FEDER) under the projects MIT-EXPL/IRA/0012/2017, POCI-01-0145-FEDER-031302, PTDC/FIS-OTI/32213/2017, EXPL/IF/00541/2015 and UIDB/04968/2020. The authors also acknowledge financial support from the European Union's Horizon 2020 research and innovation programme under the Marie Skłodowska-Curie grant agreement No. 734801 (MAGNAMED Project). The Portuguese team acknowledges the Network of Extreme Conditions Laboratories-NECL support through the project NORTE-01-0145-FEDER-022096. D.N. acknowledges the Spanish Ministry for Science, Innovation and Universities, for funding through the "Ramón y Cajal" program RYC-2017-22820. C.G. acknowledges the financial support received by ANID FONDECYT/REGULAR 1201102, ANID FONDEQUIP EQM140161, and ANID PIA/APOYO AFB180002.

Author contributions

A.S.S., I.J.S., G.N.K., H.C. and D.N. designed the study. C.G. fabricated the samples. A.S.S., S.P.S., S.A.B. performed the measurements. A.S.S., S.A.B., C.G. and G.N.K. discussed the interpretation and the relevance of the FMR-VNA results. A.S.S., I.J.S., H.C. and D.N. discussed the interpretation and the relevance of the pump-probe results. The manuscript was written through the contributions from all the authors. All the authors have given approval to the final version of the manuscript.

Competing interests

The authors declare no competing interests.

Additional information

Correspondence and requests for materials should be addressed to D.N.

Reprints and permissions information is available at www.nature.com/reprints.

Publisher's note Springer Nature remains neutral with regard to jurisdictional claims in published maps and institutional affiliations.



Open Access This article is licensed under a Creative Commons Attribution 4.0 International License, which permits use, sharing, adaptation, distribution and reproduction in any medium or format, as long as you give appropriate credit to the original author(s) and the source, provide a link to the Creative Commons licence, and indicate if changes were made. The images or other third party material in this article are included in the article's Creative Commons licence, unless indicated otherwise in a credit line to the material. If material is not included in the article's Creative Commons licence and your intended use is not permitted by statutory regulation or exceeds the permitted use, you will need to obtain permission directly from the copyright holder. To view a copy of this licence, visit <http://creativecommons.org/licenses/by/4.0/>.

© The Author(s) 2021